Energy-Efficient Europium-Based 2D Perovskite ReRAM for Photo-Tunable Neuromorphic Computing

Manvendra Chauhan and Satinder K. Sharma, *Senior Member, IEEE*

***Abstract*—Neuromorphic systems require energy-efficient non-volatile memories (NVMs) with electrical and optical tunability. We demonstrate phototunable bipolar resistive switching (RS) in Ag/$(PEA)_3$ $EuBr_6$/FTO devices using a 2D Eu-based perovskite switching layer (SL). The devices displayed forming-free operation with low SET/RESET voltages ($\pm$0.48 V in dark, $\pm$0.42 V under 365 nm illumination). UV illumination enhances the memory window ($\sim 3.0\times10^3$ to $\sim 4.8 \times 10^3$) and exhibited improved endurance and retention properties. Synaptic behaviors, including potentiation/depression and EPSC responses, exhibit higher linearity and expanded dynamic range under optical bias. Ultralow switching energies (0.62/0.27 pJ in dark; 1.23/0.17 pJ under UV) highlight the efficiency of this system. These results establish Eu-based 2D perovskites as promising, eco-friendly candidates for phototunable neuromorphic memory.**

***Index Terms*—2D perovskite, artificial synapse, lead-free, Europium.**

I. Introduction

THE scaling limits of conventional CMOS and the surging demand for low-power intelligent technology have accelerated the exploration of emerging NVMs. Resistive RAM (ReRAM) is particularly promising due to its simple architecture, fast switching, and suitability for neuromorphic computing. The International Roadmap for Devices and Systems (IRDS) emphasizes that next-generation memory must provide multifunctional and multimodal operation beyond binary storage. In this context, dual mode enabled by both electrical and optical programmability offers distinct advantages; optical stimulation facilitates low-voltage switching, enhances synaptic functionalities, and offers dual control over resistive states, thereby complementing conventional electrical programming [1], [2], [3].

Photoactive halide perovskites are promising in this regard, owing to their strong absorption, tunable electronic structure, and efficient ion migration pathways. Although 3D perovskites such as $MAPbI_3$ [4] and $MAFAPbI_3$ [1] exhibit photo-assisted switching, their long-term stability and lead content limit practical deployment. Parallel developments across the broader optoelectronic memristor landscape, ranging from photocarrier-coupled oxide systems (ZnO_{1-x}/AlO_y) [5], plasmonics-assisted devices enabling multi-wavelength recognition [6], and polymer-semiconductor nanocomposites for photosensitive switching [7], to transparent CMOS-compatible oxide stacks ($ITO/HfO_2/TiO_2$) [8] and 2D layered materials such as black phosphorus, underscore the diverse mechanisms available for light-modulated conductance tuning [9]. Recent reviews place halide-perovskite opto-memristors within this wider spectrum involving photogating, photovoltaic/diode-poling, plasmonic enhancement, and photo-ionic coupling pathways [10].

Within this context, 2D perovskites containing bulky organic cations (e.g., PEA^+) offer improved environmental stability and reduced halide migration compared to their 3D counterparts [11], enabling uniform filament dynamics and forming-free operation. Europium-based 2D halide perovskites further provide a Pb-free, structurally robust platform, aided by the close ionic-radius match between Eu^{3+} [12] and Pb^{2+} [13] and the redox stability of Eu^{3+}. Building on recent progress in dual-mode ReRAM, we report Ag/$(PEA)_3EuBr_6$/FTO devices that exhibit forming-free bipolar RS with pronounced improvements in operating voltage, memory window, and synaptic plasticity under UV illumination, demonstrating that ECM-type Ag filamentation in Eu-based 2D perovskites can be effectively modulated by optical excitation for phototunable neuromorphic memory.

II. Experimental

A 2D perovskite precursor solution was prepared by dissolving PEABr and $EuBr_3$ (3:1 molar ratio) in DMF:DMSO (9:1 v/v), and stirring at 70 °C (3000 rpm, 4 h). ReRAM devices were fabricated on FTO/glass substrates, sequentially cleaned by ultrasonication in DI water, acetone, and isopropanol (15 min each), followed by UV-ozone (30 min). The precursor was spin-coated at 6000 rpm for 50 s with toluene anti-solvent quenching, forming uniform $(PEA)_3EuBr_6$ films. Post-deposition, films were baked at 90 °C (30 min) and annealed at 100 °C (5 min). All steps were performed in an N_2-filled glovebox. Ag top electrodes (TEs) were deposited by thermal evaporation through a shadow mask, yielding Ag/$(PEA)_3EuBr_6$/FTO structures with FTO as the bottom electrode (BE). The active device area was 0.0025 cm^2.

Received 3 September 2025; revised 15 October 2025; accepted 29 October 2025. Date of publication 10 November 2025; date of current version 9 December 2025. *(Corresponding author: Satinder K. Sharma.)*

The authors are with the School of Computing and Electrical Engineering (SCEE), Indian Institute of Technology Mandi (IIT Mandi), Mandi, Himachal Pradesh 175005, India (e-mail: satinder@iitmandi.ac.in).

Color versions of one or more figures in this letter are available at https://doi.org/10.1109/LPT.2025.3631106.

Digital Object Identifier 10.1109/LPT.2025.3631106

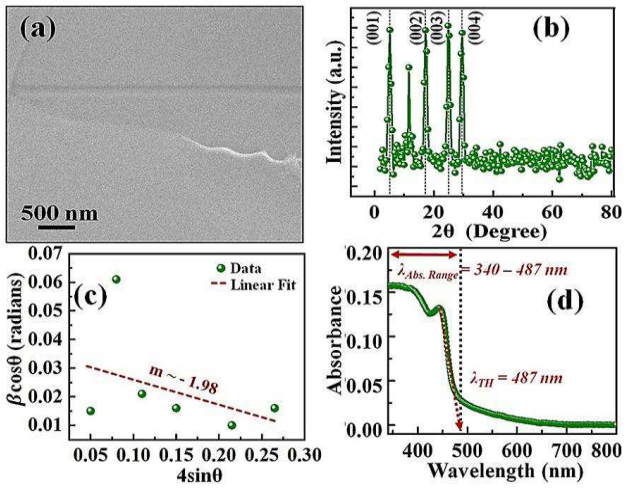

Fig. 1. Structural and optical characterization of the 2D $(PEA)_3EuBr_6$ thin film: (a) FESEM micrograph, (b) XRD with clear (00ℓ) reflections confirming c-axis stacking, (c) Williamson–Hall fit indicating crystallite size and compressive strain, (d) UV–Vis absorption spectrum.

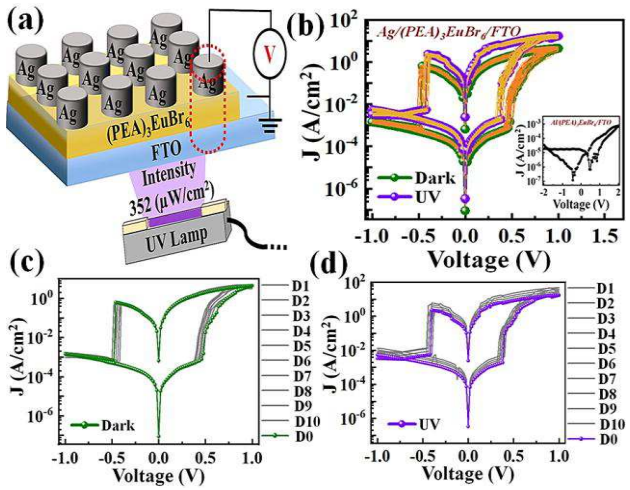

Fig. 2. (a) Schematic of the measurement set-up, (b) The consecutive (Fifty) J-V curves under dark and UV illumination (λ = 365 nm, 352 μW cm^{-2}), showing stable RS with reduced SET/RESET voltages and enhanced memory window; inset: J-V response of Al/$(PEA)_3EuBr_6$/FTO device, exhibiting monotonic analog conduction without bi-stable switching, (c-d) D2D reproducibility across 10 randomly selected cells (D1–D10) and the original (D0).

III. Results and Discussion

The plan-view FESEM micrograph of the 2D $(PEA)_3EuBr_6$ thin film in Fig. 1(a) shows a continuous, uniform, and crack-free surface on the FTO substrate. This uniformity is attributed to the PEABr:$EuBr_3$ molar ratio of 3:1, where excess PEA^+ cations terminate grain boundaries and suppress parasitic secondary phases. Such smooth, laterally homogeneous morphology is essential for RS performance, as it minimizes local field hot-spots and ensures well-defined pathways for filament formation/rupture.

XRD analysis further confirms phase purity and structural ordering. In Fig. 1(b) diffractogram displays a clear (00ℓ) ladder, with the (001) reflections at $2\theta \sim 5.2^o$ (d = 16.98 Å). The (002) and (003) peaks give consistent ℓ·d values of 22.1-22.9 Å at higher angles (18-30°), defining a repeat period of ~ 22.1 Å; the slightly lower (001) product arises from uncertainty at very low 2θ. These reflections originate from the periodic stacking of $[EuBr_6]$ octahedra and PEA bilayers along the c-axis, confirming strong Ruddlesden-Popper (RP) type out-of-plane orientation [11]. SnO_2 peaks from the FTO substrate (26.6°, 33.9°, 37.9°, 51.8°) were excluded from indexing [14].

To evaluate structural coherence, Lorentzian fitting of the dominant RP peaks was performed prior to Williamson-Hall (W-H) analysis [Fig. 1(c)]. The (001)-(004) reflections, along with weak $EuBr_3$ features near 11.0° and 12.4°, yielded FWHM values used in the W-H plot ($\beta\cos\theta$ vs $4\sin\theta$), giving a compressive strain of −1.98% and an average crystallite size of ~38.8 nm. The sharp (001) peak and limited broadening indicate high crystalline quality. The compressive strain likely originates from a mismatch between the inorganic slabs and the bulky PEA^+ layers [15], yet the extracted domain size confirms long-range stacking essential for stable RS.

The UV-vis absorption spectrum of the $(PEA)_3EuBr_6$ thin film [Fig. 1(d)] shows a well-defined edge from 340-487 nm, with a threshold near 487 nm. This sharp onset supports the photo-responsiveness of the device, as photons with λ < 487 nm efficiently modulate conducting-filament (CF) dynamics during UV-assisted switching.

Following structural evaluation, the RS behavior of Ag/$(PEA)_3EuBr_6$/FTO devices was examined using a Keithley 4200-SCS system, with Ag as the DC-biased TE and FTO grounded [Fig. 2(a)]. The J-V curves [Fig. 2(b)] confirm stable bipolar RS under both dark and UV excitation (λ = 365 nm, 352 μW cm^{-2}). Fifty consecutive dual-sweep cycles were performed under identical conditions, and overlays confirm strong cycle-to-cycle (C2C) reproducibility. UV exposure lowers the SET/RESET voltages from ±0.48 V to ±0.42 V, as photoexcited carriers in the $[EuBr_6]^{3-}$ network reduce the cation migration barrier and ease filament formation/rupture. The memory window increases from ~ 3.0×10^3 (dark) to ~ 4.8×10^3 (UV), a ~ 1.58× improvement, arising from strengthened filament pathways in the LRS and reduced trap-assisted leakage in the HRS [16], [17]. These results highlight how combined electrical and optical bias sharpens state contrast and reduces operating voltage, enabling efficient low-voltage RS in Eu-based 2D perovskite devices.

Device-to-device (D2D) reproducibility was evaluated across ten randomly selected Ag/$(PEA)_3EuBr_6$/FTO cells (D1-D10) and the reference device (D0) under dark and UV excitation (365 nm) [Fig. 2(c-d)]. Across devices, the bipolar hysteresis is consistent, with SET/RESET thresholds clustered near ±0.48 V in the dark (Fig. 2c) and ±0.42 V under UV (Fig. 2d). The inter-device dispersion of V_SET/V_RESET remains modest (dark: ~ ±28 mV; UV: ~ ±70 mV i.e. slightly larger), and loop shapes as well as threshold slopes are qualitatively similar with no irregular cycles. All devices show clear LRS/HRS separation, with UV providing systematically higher contrast, confirming reproducible RS across the array.

To validate the switching mechanism, Al was employed as an alternative TE owing to its work function (4.06-4.26 eV), comparable to Ag (~ 4.26 eV), ensuring similar energy-level

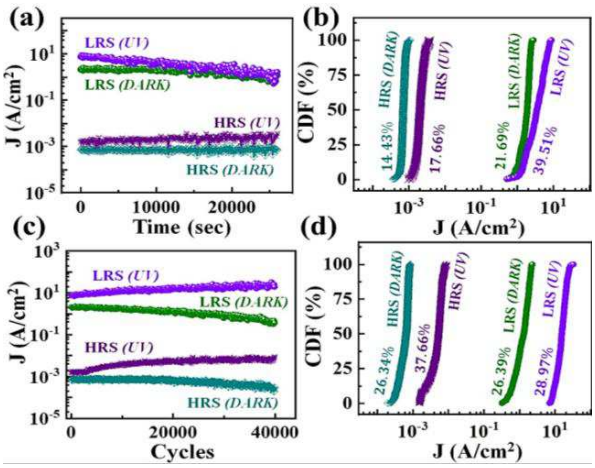

Fig. 3. Reliability characteristics of Ag/$(PEA)_3EuBr_6$/FTO devices under dark and UV illumination (λ = 365 nm). (a) Retention stability of LRS and HRS states, (b) CDF % plot extracted from retention data showing σ/μ variability for LRS and HRS current densities, (c) Endurance performance under dark and UV illumination, and (d) CDF % plot extracted from endurance data showing σ/μ% variability for LRS and HRS current densities.

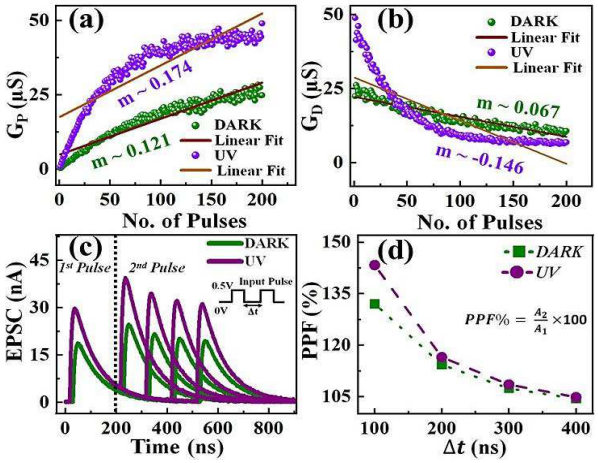

Fig. 4. Synaptic plasticity in Ag/$(PEA)_3EuBr_6$/FTO devices under dark and UV illumination. (a) linearly fitted Potentiation indicating learning rate and (b) linearly fitted depression curves indicating forgetting rate, (c) EPSC responses. (d) PPF% index as a function of pulse interval (Δt).

alignment while eliminating electrochemically active cation migration. Unlike Ag devices, Al-based cells show no abrupt SET/RESET but only a gradual rise in current without a memory window [Fig. 2(b), inset]. This behavior stems from the electrochemical inertness of Al; a native AlO_X interlayer blocks ion exchange and suppresses the mobile cation reservoir needed for filament growth. Given that 2D PEA-based lattices already hinder halide migration relative to 3D analogues, the absence of bistability in Al devices rules out vacancy-mediated switching. The sharp, low-voltage RS observed only with Ag devices confirms that these devices operate via an electrochemical metallization (ECM) mechanism.

Afterwards, the retention behavior of the Ag/$(PEA)_3EuBr_6$/FTO ReRAM was assessed by programming the device into LRS and HRS states and monitoring stability up to 26,000 s at a read voltage of 0.2 V [Fig. 3(a)]. Both states remained stable under dark and illuminated (365 nm) conditions. In the dark, the mean LRS/HRS ratio was ~2485.03, while under illumination, it decreased slightly to ~1819.41, attributable to photo-induced carrier accumulation and trap-assisted recombination during prolonged UV exposure, which gradually weakens LRS/HRS contrast [1], [3].

Switching consistency was further quantified via cumulative distribution function (CDF) plots [Fig. 3(b)], yielding σ/μ variability of 21.69% (dark) and 39.51% (UV) for LRS, and 14.43% (dark) and 17.66% (UV) for HRS.

The endurance performance [Fig. 3(c)] demonstrates that the devices maintain stable cycling, with UV illumination providing a clear improvement. Over 40,000 cycles, the average LRS/HRS ratio increases from ~2159.74 (dark) to ~3190.49 (UV), a ~ 1.47× enhancement arising from a stronger photo-induced rise in LRS (~ 12.30×) compared to HRS (~ 8.33×). In the dark, both states gradually drift downward due to partial relaxation of the ECM filament, charge trapping in the perovskite, and slow redox equilibration, which collectively thin the conductive path (reducing LRS) and increase the barrier in HRS [18]. Under UV (365 nm), this trend reverses: photo-ionic coupling and persistent photoconductivity increase carrier density and lower the overpotential for Ag^+ migration, enabling thicker or more stable CFs and easier re-nucleation. Light-assisted ion motion also mitigates trap-limited leakage, shifting both states toward higher conductance [10].

Cycle-to-cycle statistics [Fig. 3(d)] give σ/μ values of 26.39% (dark) and 28.97% (UV) for LRS and 26.34% (dark) and 37.66% (UV) for HRS, confirming modest variability. Overall, the Ag/$(PEA)_3EuBr_6$/FTO device exhibits robust state stability under dark and UV-assisted operations.

Neuromorphic functionality was evaluated through potentiation-depression measurements, which emulate long-term synaptic plasticity. Successive positive voltage pulses induce potentiation (learning), while negative pulses drive depression (forgetting), with conductance evolution recorded in each case. A train of 100 consecutive voltage pulses (±0.5 V amplitude, 100 ns pulse width t_W, 100 ns interpulse interval (Δt)) was applied to the devices. As shown in Fig. 4(a-b), for the Eu-based 2D perovskite ReRAM, the potentiation slope under dark conditions was ~ 0.121 μS/pulse, while the depression slope was −0.067 μS/pulse. Under UV illumination, the potentiation slope increased to ~ 0.174 μS/pulse and the depression slope steepened to −0.146 μS/pulse.

These results confirm that photo excitation accelerates both synaptic potentiation and depression, broadening the tunability of synaptic weights. The steeper depression slope under UV likely stems from thicker Ag filaments that, once destabilized, rupture more abruptly due to photo-assisted ion migration. Such modulation is advantageous for light-assisted neuromorphic systems requiring rapid and reversible weight updates. Beyond slope analysis, the dynamic range ($DR_{dB} = 20log_{10}(G_{max}/G_{min})$) increased from ~ 9.5 dB (dark) to ~ 18.0 dB (UV), indicating that UV-assisted Ag^+ migration strengthens filament growth and rupture, widens the conductance window, and supports finer multilevel tuning.

The switching energy per pulse was estimated using the standard relation, $E = \int VIdt \approx V^2Gt_W$, where G is the device conductance during the pulse. At the 200th pulse

(0.5 V, t_W = 100 ns), potentiation conductance of 24.87 μS (dark) and 49.05 μS (UV) correspond to ~ 0.62 pJ and ~ 1.23 pJ, while depression conductance of 10.68 μS (dark) and 6.839 μS (UV) yield ~ 0.27 pJ and ~ 0.17 pJ energy per pulse. These picojoule-scale operations show that optical excitation increases potentiation energy but reduces depression energy, enabling asymmetric and controllable power usage. To our knowledge, this represents the first demonstration of pJ-level operation in Eu-based 2D perovskite memristors. EPSC measurements further confirm short-term plasticity through paired-pulse facilitation (PPF) [Fig. 4(c)]. In the dark, the device shows $A_2 > A_1$ with a facilitation index of 132.0% at Δt = 100 ns, decreasing to 104.3% at Δt = 400 ns. Under UV, both A_1 and A_2 increase due to photo-assisted carrier generation and faster Ag^+ migration, while the relative PPF ratio remains nearly unchanged (143.3% at Δt = 100 ns, 104.8% at Δt = 400 ns), as shown in Fig. 4(d). Thus, optical bias enhances synaptic strength without disturbing temporal fidelity. Together with long-term plasticity, these results establish Eu-based 2D perovskite ReRAM as a promising platform for light-responsive multimodal neuromorphic systems.

IV. Conclusion

This work establishes $(PEA)_3EuBr_6$ SL as a multifunctional switching medium for phototunable ReRAM. Ag/$(PEA)_3EuBr_6$/FTO devices exhibit bipolar RS with reduced SET/RESET voltages under UV ($\pm$0.42 V vs. $\pm$0.48 V), an expanded memory window (~ 3.0×10^3 to ~ 4.8×10^3), endurance ~ 40,000 cycles, and retention ~ 26,000 secs. Neuromorphic analysis verifies photo-tunable plasticity, with steeper potentiation/depression slopes and a widened DR_{db} (9.5 dB to 18 dB). EPSC studies show that UV strengthens transient responses without compromising timing accuracy. Crucially, picojoule-level operation (~0.62/1.23 pJ for potentiation, ~0.27/0.17 pJ for depression in dark/UV) highlights their suitability for low-voltage, energy-efficient, multimodal memory and neuromorphic applications.

Acknowledgment

The authors gratefully acknowledge the C4DFED Facility, IIT Mandi, for access to the Class 100 cleanroom and facilities supporting device fabrication, FESEM nanoscale imaging, and electrical measurements. They also thank AMRC, IIT Mandi, for chemical characterization support.

References

[1] M. Chauhan, R. Singh, and S. K. Sharma, "Electro-optically tunable passivated double-cation perovskite-based ReRAM for low-power memory applications," *ACS Appl. Electron. Mater.*, vol. 6, no. 4, pp. 2709–2719, Apr. 2024, doi: 10.1021/acsaelm.4c00257.

[2] H. Wang et al., "Optical–electrical coordinately modulated memristor based on 2D ferroelectric RP perovskite for artificial vision applications," *Adv. Sci.*, vol. 11, no. 33, Sep. 2024, Art. no. 2403150, doi: 10.1002/advs.202403150.

[3] M. Chauhan and S. K. Sharma, "High-performance perovskite-inspired lanthanohalide memristors for phototunable neuromorphic applications," *IEEE Trans. Electron Devices*, vol. 72, no. 8, pp. 4549–4557, Aug. 2025, doi: 10.1109/TED.2025.3584289.

[4] G. Lin et al., "An organic–inorganic hybrid perovskite logic gate for better computing," *J. Mater. Chem. C*, vol. 3, no. 41, pp. 10793–10798, 2015, doi: 10.1039/c5tc02270c.

[5] D.-C. Hu, R. Yang, L. Jiang, and X. Guo, "Memristive synapses with photoelectric plasticity realized in ZnO_{1-x}/AlO_y Heterojunction," *ACS Appl. Mater. Interfaces*, vol. 10, no. 7, pp. 6463–6470, Feb. 2018, doi: 10.1021/acsami.8b01036.

[6] J. Han et al., "Multi-wavelength-recognizable memristive devices via surface plasmon resonance effect for color visual system," *Small*, vol. 19, no. 23, Jun. 2023, Art. no. e2207928, doi: 10.1002/smll.202207928.

[7] A. D. Trofimov et al., "Photosensitive resistive switching in parylene–PbTe nanocomposite memristors for neuromorphic computing," *Nanoscale*, vol. 17, no. 14, pp. 8484–8495, Apr. 2025, doi: 10.1039/d5nr00456j.

[8] F. Wu, C.-H. Chou, and T.-Y. Tseng, "CMOS-compatible memristor for optoelectronic neuromorphic computing," *Nanosc. Res. Lett.*, vol. 17, no. 1, p. 105, Nov. 2022, doi: 10.1186/s11671-022-03744-x.

[9] Y. Zhou et al., "Black phosphorus based multicolor light-modulated transparent memristor with enhanced resistive switching performance," *ACS Appl. Mater. Interfaces*, vol. 12, no. 22, pp. 25108–25114, Jun. 2020, doi: 10.1021/acsami.0c04493.

[10] X. Zhang et al., "Halide perovskite memristors for optoelectronic memory and computing applications," *Inf. Funct. Mater.*, vol. 1, no. 3, pp. 265–281, Dec. 2024, doi: 10.1002/ifm2.23.

[11] Y. Chen, Y. Sun, J. Peng, J. Tang, K. Zheng, and Z. Liang, "2D Ruddlesden–Popper perovskites for optoelectronics," *Adv. Mater.*, vol. 30, no. 2, Jan. 2018, Art. no. 1703487, doi: 10.1002/adma.201703487.

[12] P. J. Dereń, D. Stefanska, M. Ptak, and P. Wisniewski, "Method to measure the degree of reduction of Eu^{3+} to Eu^{2+}: How anion and cation vacancies influence the degree of reduction," *J. Phys. Chem. C*, vol. 125, no. 44, pp. 24505–24514, Nov. 2021, doi: 10.1021/acs.jpcc.1c06977.

[13] M. Kirberger and J. J. Yang, "Structural differences between Pb^{2+}- and Ca^{2+}-binding sites in proteins: Implications with respect to toxicity," *J. Inorganic Biochem.*, vol. 102, no. 10, pp. 1901–1909, Oct. 2008, doi: 10.1016/j.jinorgbio.2008.06.014.

[14] L.-Y. Zhu et al., "Hierarchical highly ordered SnO_2 nanobowl branched ZnO nanowires for ultrasensitive and selective hydrogen sulfide gas sensing," *Microsyst. Nanoeng.*, vol. 6, no. 1, p. 30, May 2020, doi: 10.1038/s41378-020-0142-6.

[15] Y. Zou et al., "Microstrain and crystal orientation variation within naked triple-cation mixed halide perovskites under heat, UV, and visible light exposure," *ACS Energy Lett.*, vol. 9, no. 2, pp. 388–399, Feb. 2024, doi: 10.1021/acsenergylett.3c02617.

[16] X. Guan et al., "A solution-processed all-perovskite memory with dual-band light response and tri-mode operation," *Adv. Funct. Mater.*, vol. 32, no. 16, Apr. 2022, Art. no. 2110975, doi: 10.1002/adfm.202110975.

[17] S. Shao and M. A. Loi, "The role of the interfaces in perovskite solar cells," *Adv. Mater. Interfaces*, vol. 7, no. 1, Jan. 2020, Art. no. 1901469, doi: 10.1002/admi.201901469.

[18] M. U. Ali, H. Mo, A. U. Rehman, T. L. Leung, and A. B. Djurišić, "Metal halide perovskites: Stability under illumination and bias," *Trends Chem.*, vol. 6, no. 5, pp. 248–259, May 2024, doi: 10.1016/j.trechm.2024.03.009.